

CMFGEN grids of atmosphere models for massive stars OB-type stars at the Magellanic Clouds

W. Marcolino¹, J.-C. Bouret², F. Martins³, and D.J Hillier⁴

¹ Universidade Federal do Rio de Janeiro, Observatório do Valongo, Ladeira Pedro Antônio, 43, CEP 20080-090, Rio de Janeiro, Brazil

² Aix Marseille Univ, CNRS, CNES, LAM, Marseille, France

³ LUPM, Université de Montpellier, CNRS, Place Eugène Bataillon, F-34095 Montpellier, France

⁴ Department of Physics and Astronomy & Pittsburgh Particle physics, Astrophysics, and Cosmology Center (PITT PACC), University of Pittsburgh, Pittsburgh, PA 15260, USA

Received / Accepted

ABSTRACT

Context. Large spectroscopic surveys of individual massive stars, such as ULLYSES and XSHOOTU, provide observational data for hundreds of massive stars. Their analysis requires large numbers of synthetic spectra so that stellar parameters can be determined. In addition, libraries of massive stars' spectra are needed to produce population synthesis models able to reproduce the observed spectra of unresolved young stellar populations, such as those revealed by the James Webb Space Telescope (JWST) in the early Universe.

Aims. Our main goal is to provide an extensive library of synthetic spectra and spectral energy distributions of OB stars at metallicities of the Magellanic Clouds. This library will offer a wealth of spectrophotometric information, making it readily applicable to a variety of astrophysical problems.

Methods. We used the CMFGEN code to calculate 606 NLTE, line-blanketed, expanding atmosphere models using a comprehensive set of atomic data. An overall metallicity of $1/2 Z_{\odot}$ and $1/5 Z_{\odot}$ was adopted for the Large Magellanic Cloud (LMC) and Small Magellanic Cloud (SMC), respectively. We produced high-resolution spectra from 30 \AA to $3 \mu\text{m}$ for stars on the Main Sequence and slightly beyond.

Results. We provide spectral energy distributions, normalized synthetic spectra, ionizing fluxes, and photometry in various bands: Johnson UB_V, Cousins RI, Bessel JHK, selected wide JWST filters, Gaia, and LSST ugrizy filters. For each of these filters, we compute bolometric corrections for all synthetic spectra and calibrations as a function of effective temperature.

Conclusions. All of our synthetic spectra are publicly available through the POLLUX database, aiming to expedite multiwavelength analyses of massive stars in low metallicity environments.

Key words. Stars: massive – Stars: atmospheres – Stars: fundamental parameters – Astronomical databases: miscellaneous

1. Introduction

Our knowledge about massive stars has greatly improved since the first modern ultraviolet observations obtained detailed P-Cygni spectral profiles (Morton 1967; Snow & Morton 1976; Hutchings 1976; Hutchings & von Rudloff 1980). It is now well established that the winds of O and B stars are mainly driven by momentum transfer of their intense radiation fields to metals present in the gas, i.e., they are line-driven winds (Lucy & Solomon 1970; Castor et al. 1975; Kudritzki et al. 1989; Puls et al. 2000). Consequently, the strength of these winds, and thus the evolutionary paths of these stars from their birth to their final fate, hinges largely on the environment's metallicity (Z). The quantitative aspects of this dependence have been the topic of numerous observational and theoretical studies and are still under thorough investigations (e.g., Leitherer et al. 1992; Bouret et al. 2003; Mokiem et al. 2007; Björklund et al. 2021; Marcolino et al. 2022; Hawcroft et al. 2024; Krtićka et al. 2024).

Recently, the ULLYSES¹ and XSHOOTU² observational programs provided an invaluable large (~ 240 targets), homogeneous dataset of spectra of massive stars in the Large (LMC) and Small (SMC) Magellanic Clouds, alongside a few targets in the Local Group galaxies NGC 3109 and Sextans A (Vink et al. 2023). These galaxies all have sub-solar metallicity, ranging approximately from $1/2$ to $1/10 Z_{\odot}$. Within ULLYSES, hundreds of Hubble Space Telescope (HST) orbits were devoted to obtain high-resolution ultraviolet spectroscopy with the Cosmic Origins Spectrograph (COS) and Space Telescope Imaging Spectrograph (STIS). On the other hand, XSHOOTU focused on high-resolution optical-near IR observations of ULLYSES targets with the XSHOOTER spectrograph on the Very Large Telescope (VLT). Other initiatives, such as BLOeM, which focuses on binaries with the VLT (Shenar et al. 2024), and the 4MOST-100IMC survey (Cioni et al. 2019), will ultimately provide thousands of near-UV to near-IR spectra of massive stars in the Magellanic Clouds. Additionally, the James Webb Space Telescope (JWST) has just opened a new window of possibilities for investigating the infrared emission characteristics of massive stars,

Send offprint requests to: Wagner Marcolino
e-mail: wagner@ov.ufrj.br

¹ <https://ullyses.stsci.edu/>

² X-shooting ULLYSES - <https://massivestars.org/xshootu/>

an area that remains poorly explored (see e.g., [Marcolino et al. 2017](#)).

Such multiwavelength observations of massive stars in various Local Group galaxies are crucial for understanding not only the quantitative effects of metallicity on stellar evolution, but also stellar populations in both nearby and distant galaxies. In this context, sophisticated, state-of-the-art atmosphere models are an indispensable component of this process.

Through the comparison of synthetic and high-resolution observed spectra, via diagnostic lines, essential physical parameters from both the photospheric and wind regions, as well as chemical abundances, can be obtained. These can then be directly compared with theoretical predictions, for example, from hydrodynamics or evolutionary calculations ([Mokiem et al. 2006, 2007](#); [Hunter et al. 2008](#); [Ramírez-Agudelo et al. 2013](#); [Markova et al. 2014](#); [Martins et al. 2015](#); [Holgado et al. 2018](#); [Markova et al. 2018](#); [Mahy et al. 2020](#); [Bouret et al. 2021](#); [de Burgos et al. 2023](#); [Martins et al. 2024](#)).

Despite considerable progress in recent decades, the modeling of the expanding atmospheres of massive stars remains a big challenge. Radiative transfer involving thousands of lines must be solved together with the statistical equilibrium equations (NLTE), as the LTE approximation is invalid. A set of highly non-linear and coupled equations must be simultaneously solved. This task is complex and computationally expensive, but paramount for a proper interpretation of observed spectra ([Hillier 2012](#)). Consequently, the availability of pre-computed grids of synthetic spectra can greatly speed-up the analysis of large samples of stars. Such libraries of spectra can serve as input for techniques relying on machine learning methods that aim at providing fundamental parameters of OB stars. A large dataset of models can be also useful in other astrophysical contexts. Realistic ionizing sources are needed for photoionization codes (e.g., to investigate spectroscopy of H II regions), a library of synthetic spectra can aid stellar population synthesis analyses, and diverse model parameters can be used as well, as input in hydrodynamic calculations (see e.g., [Vink et al. 2001](#)).

Grids of synthetic spectra for massive stars are publicly available. [Lanz & Hubeny \(2003\)](#) and [Lanz & Hubeny \(2007\)](#) present models for O and B stars respectively. The computations were performed with the code TLUSTY ([Hubeny & Lanz 1995](#)) and cover metallicities from twice solar to zero. The specificity of these grids is that they do not take spherical extension and stellar winds into account. The library of O stars synthetic spectra presented by [Eldridge et al. \(2017\)](#) overcome this limitation. The atmosphere code WM-BASIC ([Pauldrach et al. 2001](#)) was used and the grid covers a wide range of metallicities (see Sect. 2.3.2 and Table 2 of [Eldridge et al. 2017](#)). However WM-BASIC spectra do not include the physics required to produce detailed line profiles in the optical range. More realistic synthetic spectra are presented in [Hainich et al. \(2019\)](#) and calculated with the PoWR code ([Gräfener et al. 2002](#); [Sander et al. 2015](#)). Solar, LMC and SMC metallicities have been chosen for these PoWR grids that also extend to the range of parameters typical of Wolf-Rayet stars ([Todt et al. 2015](#); [Sander et al. 2012](#)).

The grids presented here are based on the CMFGEN code ([Hillier & Miller 1998](#)) which is widely used for the spectroscopic analysis of massive stars, from the EUV to the infrared (e.g., [Hillier et al. 2003](#); [Martins et al. 2005](#); [Marcolino et al. 2009](#); [Martins et al. 2015](#); [Marcolino et al. 2017](#); [de Almeida et al. 2019](#); [Bouret et al. 2021](#)). Libraries of synthetic spectra at solar and sub-solar metallicity are already available through

the POLLUX database³. [Zsargó et al. \(2020\)](#) also provide large model grids with special focus on wind properties. However these libraries do not follow the classical parameter coverage of grids, i.e. do not have a regular sampling in effective temperature and surface gravity. Rather, they correspond to spectra computed along evolutionary tracks ([Martins & Palacios 2017, 2021, 2022](#); [Zsargó et al. 2020](#)). Here we complement these data by proper grids of models at sub-solar metallicity. We generated a total of 606 models based on the CMFGEN code, from which we produced high-resolution spectra from the EUV to mid-IR. In addition to synthetic spectra, we provide synthetic photometry, bolometric corrections, and ionizing fluxes. We make all spectra publicly available at the POLLUX database.

The paper is organized as follows. In Sect. 2 we describe in detail how we constructed our grids. Sect. 3 presents the spectrophotometric data we generated. We discuss the main characteristics, magnitudes and bolometric corrections in different filters, as well as the ionizing radiation in this section. Finally, we summarize the main conclusions of our paper in Sect. 4.

2. Building the grids

2.1. CMFGEN: Main ingredients

The grids were constructed using the CMFGEN code by [Hillier & Miller \(1998\)](#). Initially, CMFGEN was designed to compute spherically symmetric expanding model atmospheres in NLTE to simulate massive, hot stars with powerful, optically thick winds. It has been since used in a great variety of cases, from OB stars with weak winds, in the Galaxy or in the Magellanic Clouds (MCs), to all types of supernovae (core-collapse and thermonuclear), Wolf-Rayet stars, Luminous Blue Variables, and central stars of planetary nebulae ([Aadland et al. 2022](#); [Blondin et al. 2015](#); [Dessart & Hillier 2005, 2015](#); [Dessart et al. 2023](#); [Groh et al. 2009, 2011](#); [Hillier 1987](#); [Hillier & Miller 1999](#); [Hillier 2020](#); [Marcolino et al. 2007b,a](#); [Martins et al. 2004](#); [Morris et al. 2017](#); [Neugent et al. 2017](#); [Teodoro et al. 2020](#)).

CMFGEN solves the radiative transfer and statistical equilibrium equations simultaneously within the co-moving frame (CMF) framework, including a treatment of line-blanketing using a super-level approach ([Hillier & Miller 1998, 1999](#)). The super-levels formalism allows for the inclusion of multiple energy levels from various ion species in the model atmosphere calculations. More details about this are given in Sect. 2.3 (see also Table 1).

The wind structure is treated in the following way: the radiative acceleration is computed from the solution of the level populations, and is used to determine in an iterative way the density structure of the inner atmosphere in a quasi-hydrostatic region. The resulting velocity law is smoothly connected to a β velocity law in the wind (see e.g., [Bouret et al. 2012](#)). The wind mass-loss rate, density, and velocity are related through the continuity equation.

To address the unstable nature of radiatively driven winds, CMFGEN can incorporate the effects of X-rays and wind clumping. The optically-thin clumping approximation is used (see e.g., [Bouret et al. 2005](#)), but the code was recently modified to include shells, handling clumps with arbitrary optical depths ([Flores & Hillier 2021](#); [Flores et al. 2023](#)). However, to facilitate the grid construction, we decided to not include clumping nor X-rays in the models. Both ingredients can be easily switched on when starting the analysis of an observed spectrum.

³ <https://pollux.oreme.org/>

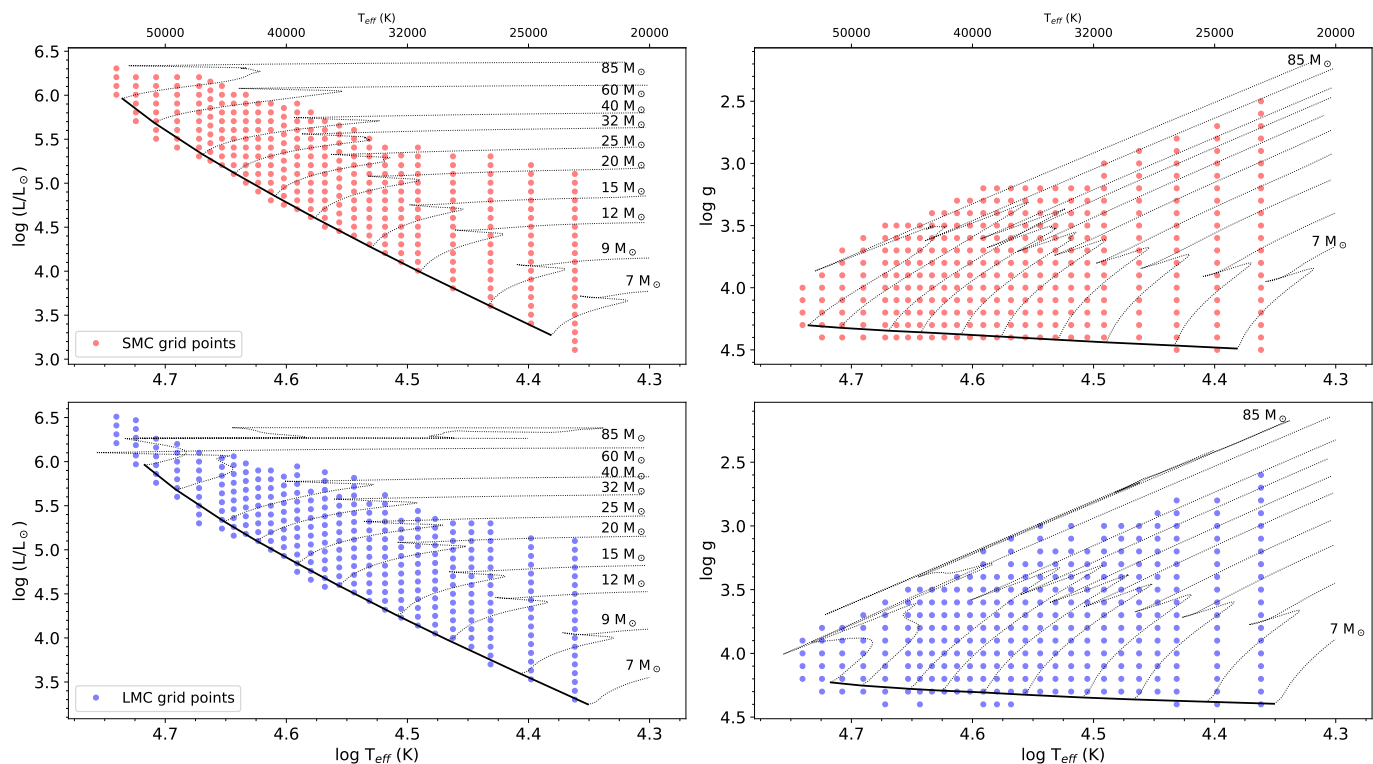


Fig. 1. SMC and LMC grid coverage in the Hertzsprung-Russell (left panels) and Kiel diagrams (right panels). Tracks from [Georgy et al. \(2013\)](#) and [Eggenberger et al. \(2021\)](#) are represented by dotted-lines. The thick solid line indicates the location of the ZAMS.

Once the atmosphere model is converged, a formal solution of the radiative transfer equation is computed in the observer’s frame, providing a synthetic spectrum for comparison with observations. In this step, CMFGEN takes into account a radially increasing microturbulent velocity, starting at about 10 km s^{-1} at the photosphere (see e.g., [Hillier et al. 2003](#), for the adopted formula) and extending up to $\sim 10\%$ of the terminal velocity in the outer atmosphere. Detailed line profiles and broadening mechanisms are taken into account.

2.2. Grid setup

The parameter space encompassed by our grids is anticipated to accurately depict the characteristics of actual OB stars in the Magellanic Clouds, aligning with recent high-resolution ultraviolet and optical observations conducted under the ULLYSES and XSHOOTU programs.

We built two grids of models, both assuming a solar helium abundance, $\text{He}/\text{H} = 0.085$ (by number). All other chemical abundances are scaled from the solar values ([Asplund et al. 2009](#)) assuming a metallicity of $1/2$ and $1/5 Z_{\odot}$ for the LMC and SMC, respectively.

The effective temperature (T_{eff}) range from 23 kK to 55 kK. Most of the grid was computed with a 1 kK step, but nearing both T_{eff} ends, a coarser step of 2kK was adopted⁴. In total, we have 25 temperatures for the SMC and 26 temperatures for the LMC. For each T_{eff} , we calculate models for a series of surface gravities ($\log g$ ’s), adopting a 0.1 dex step. The first value of $\log g$ and $\log L/L_{\odot}$ of the grid are the rounded value of $\log g$ on the zero-age main-sequence (ZAMS) (1st point) for Geneva models

⁴ Less ULLYSES targets are expected towards these effective temperatures (see e.g., Fig. 2 of [Vink et al. 2023](#)).

(from [Georgy et al. 2013](#) and [Eggenberger et al. 2021](#)). Then, as we decrease $\log g$ by 0.1 dex, we increase $\log L/L_{\odot}$ by 0.1 dex. For example, for a first model with $\log L/L_{\odot} = 5.0$ for $\log g = 4.4$, the second model in the series will have $\log L/L_{\odot} = 5.1$ for $\log g = 4.3$, and so on. This approach is equivalent to leaving the mass unchanged for a sequence of models with fixed T_{eff} . The aim of this empirical sampling in $\log g$ (or equivalently $\log L/L_{\odot}$) is to sample the main-sequence (MS) and a little beyond for a given T_{eff} (i.e. to make a “vertical line” covering enough of the MS in the HRD).

We assumed a fixed micro turbulence velocity of 10 km s^{-1} . The wind acceleration parameter is set to $\beta = 1.0$ and the mass-loss rates are computed using the [Vink et al. \(2001\)](#) formula for the corresponding metallicity, assuming that the terminal velocity is proportional to the escape velocity as $v_{\infty}/v_{\text{esc}} = 3.0$, to be consistent with [Martins & Palacios \(2021\)](#) and references therein. Other mass-loss recipes exist. However, there is no consensus on which one is preferable. For example, the predictions for the mass-loss rate dependence with luminosity (and metallicity) scatter (see e.g., fig. 5 of [Björklund et al. 2021](#)). Vink’s recipe remains the most widely used in evolutionary calculations. As previously mentioned, our initial model grid points were anchored to ZAMS track points that utilize Vink.

We present the LMC and SMC grid coverage in the Hertzsprung-Russell and Kiel diagrams in Fig. 1. Our points, each corresponding to an atmosphere model, are shown along with theoretical tracks from [Georgy et al. \(2013\)](#) and [Eggenberger et al. \(2021\)](#), that include rotation. We stress that our models are not tailored to follow the tracks and the latter are shown for illustration purpose. A large interval of initial mass is covered for each metallicity, representing both O and B stars. For several masses, the points sample well the whole Main Sequence.

Table 1. Ions, number of super-levels and number of levels included in the model calculations. Ions with an asterisk symbol are only used in low or high T_{eff} models.

Ion	# super-levels	# levels
H I	30	30
He I	69	69
He II	30	30
C II*	92	322
C III	99	243
C IV	64	64
N II*	59	105
N III	57	287
N IV	44	70
N V	41	49
O II*	155	274
O III	36	104
O IV	30	64
O V	32	56
O VI*	9	15
Ne II	14	48
Ne III	23	71
Ne IV	17	52
Ne V	37	166
Mg II	36	44
Si II*	27	53
Si III	50	50
Si IV	66	66
S III	39	78
S IV	40	108
S V	37	144
S VI*	28	58
Ar III	24	138
Ar IV	30	102
Ar V	14	29
Ar VI*	21	81
Ca III	29	88
Ca IV	19	72
Ca V*	10	613
Fe II*	24	295
Fe III	65	607
Fe IV	100	1000
Fe V	139	1000
Fe VI	59	1000
Fe VII*	41	252
Ni II*	27	158
Ni III	24	150
Ni IV	36	200
Ni V	46	183
Ni VI	40	182
Ni VII*	37	308

We note that both grids may be updated in the future, for instance, by filling gaps in temperature, adding more ions, and extending the mass range. For instance, it is certainly worth exploring models above $100 M_{\odot}$. Despite being extremely rare, very massive stars (VMS) have been observed, modeled, and have been shown to be crucial for population synthesis studies in nearby galaxies (see e.g., [Martins et al. 2023](#), and references therein). Grid points for VMS are beyond the scope of the present paper, but models and spectra along evolutionary tracks

have been computed in the literature (see e.g., [Martins & Palacios 2022](#)).

2.3. Atomic data

OB stars exhibit a rich ultraviolet spectrum characterized by numerous metallic absorption lines (e.g., [Pauldrach et al. 1993](#)). Primarily originating from the photosphere (e.g., iron forest), these lines are often accompanied by prominent wind P-Cygni profiles (e.g., C IV λ 1549, N V λ 1240, O V λ 1371) that are important diagnostics of the mass-loss rate and the outflow velocity structure. Conversely, their optical spectra are dominated mainly by strong hydrogen and helium lines. These are in general observed in absorption, but some may be in emission depending on the wind strength (e.g. H α in supergiants).

Spectral analyses that neglect elements other than H, He, and CNO, inaccurately infer important physical parameters. The presence of numerous metal lines blocks and scatter back radiation to inner parts of the atmosphere, resulting in a back-warming, implying a change in the ionization structure of a model in comparison with, for example, a metal free one (see e.g., [Martins et al. 2002](#); [Lanz & Hubeny 2003, 2007](#)). In fact, models with the same effective temperature but different metallicities can impact He I-II line strengths ([Martins et al. 2002](#)).

In our grids, we choose to incorporate as many elements and ions as possible, having a compromise with an appropriate amount of blanketing (e.g., CNO+iron elements ions) and a manageable model, i.e., not too large and very computationally expensive. We present the dataset used in Table 1. A total of 2046 super-levels were formed from a total of 9178 levels (for more details, see [Hillier & Miller 1998](#)). In practice, they correspond up to hundreds of thousands transitions to be taken care of in the radiative transfer calculation.

2.4. Availability and output products

The 606 spectra of our grids are made publicly available at the POLLUX database⁵ ([Palacios et al. 2010](#)). The entire SED can be downloaded, as well as cuts of the UV, visible and infrared spectrum. A quick look tool with zoom facilities allows inspections of specific features prior to download. For each file a header describes the atmosphere model parameters and the parameters of the formal solution of the radiative transfer that lead to the synthetic spectra. The non-normalized and normalized spectra can be directly compared to observations, after including the necessary natural and instrumental broadening effects. We recall that CMFGEN calculates a spectrum in the reference frame of an observer at 1 kpc, by default. Thus, a proper distance scaling and addition of ISM extinction effects must be taken into account when handling the non-normalized data. The atmosphere models are available upon request. They can be used to construct new ones or to obtain several important physical properties of the atmosphere – for instance, ionization structures, level populations – which are relevant for various purposes.

3. Spectrophotometric data

3.1. Synthetic high-resolution spectra

We generated high-resolution spectra spanning from extreme ultraviolet (EUV) to mid-infrared (mid-IR) for all models within

⁵ <https://pollux.oreme.org>

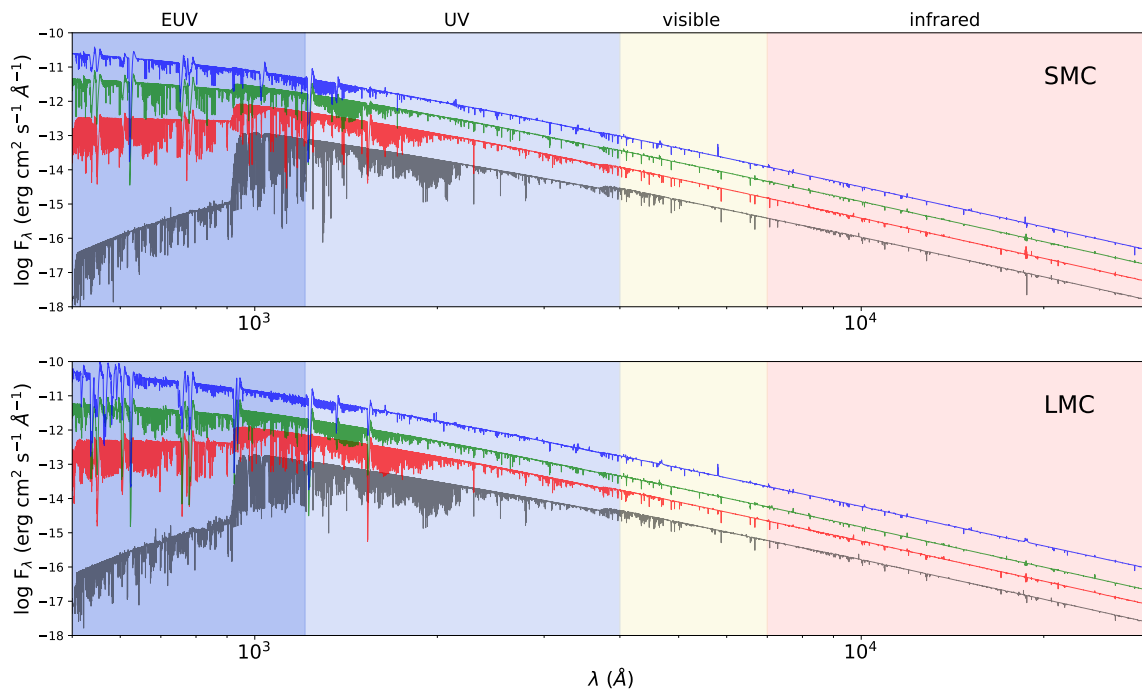


Fig. 2. Illustrative spectra from our grid of models representing LMC and SMC OB stars. The displayed wavelength range spans from 500\AA to 30000\AA . All models have a fixed $\log g = 4.0$ and $T_{\text{eff}} = 25, 35, 45$ and 55kK (bottom to top). Roughly, they correspond to an early B star, late, mid and early O star, respectively. Background colors correspond to different wavelength ranges as indicated by the top labels.

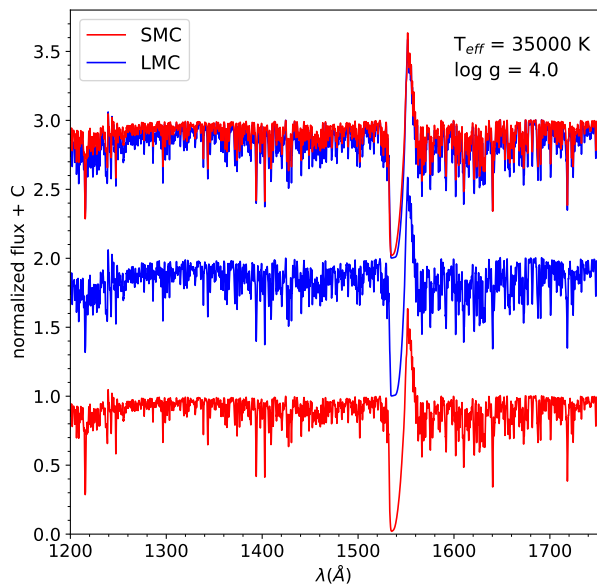


Fig. 3. Zoom on the far-UV spectrum of two models with similar T_{eff} and $\log g$ but different metallicities (hence wind parameters). The blue (red) spectrum is the LMC (SMC) model. The spectra were convolved with a rotational profile of 100 km s^{-1} and a resolving power $R = 50000$.

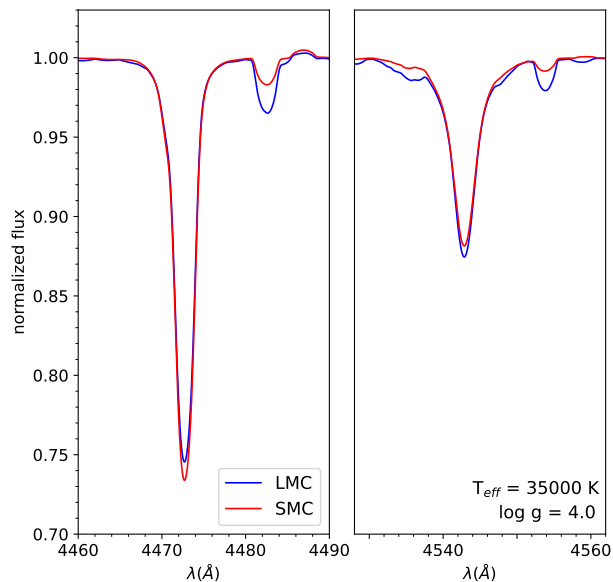


Fig. 4. Same as for Fig. 3, but for the optical lines He I 4471 (left panel) and He II 4542 (right panel).

the LMC and SMC grids. These spectra can yield several relevant physical parameters, some of which will be discussed in the next sections.

In Fig. 2 we present a small set of spectra to illustrate the quality of the models, over a large wavelength interval. They have $\log g = 4.0$ and the effective temperature T_{eff} is 25, 35, 45 and 55kK , from bottom to top. The fluxes are absolute and

were scaled taking into account the LMC and SMC distances (Pietrzyński et al. 2019; Graczyk et al. 2020; Vink et al. 2023). No reddening or extinction is simulated.

The highest flux and density of wind and photospheric lines in the EUV/UV is apparent, a common characteristic of OB stars. Overall, the LMC models present more absorption features than the SMC ones, reflecting the higher metallicity. Hundreds of lines from the EUV to the infrared can be seen and readily compared with real observed spectra, after the appropriate rotational, macroturbulence, and/or instrumental convolution.

Figure 3 shows how metallicity directly impacts the far-UV spectra for models with similar fundamental parameters. The iron line forests that make most of the absorption features in that figure are weaker at lower Z . Helium lines are also impacted by the indirect metallicity effects of line-blocking and back-warming. We see in Fig. 4 that even if the He/H ratio is unchanged between both grids, the He I 4471 line is weaker at higher Z , while the He II 4542 line is stronger. This is due to the different temperature structure at different metallicity (see Martins et al. 2002; Repolust et al. 2004 for details). These lines are key features to constrain T_{eff} in spectroscopic analysis.

In the Appendix, we show additional spectra from our grid models across selected wavelength intervals, highlighting their practical significance. Figure A.1 focus on the UV/EUV range, its richness and changes due to the metallicity. Figure A.2 illustrates the effects of T_{eff} and $\log g$ variations on selected hydrogen and helium lines. In Fig. A.3 we provide examples of infrared spectra.

3.2. Photometry

The spectra of our model grids were computed over a large wavelength interval, thus allowing the calculation of magnitudes in various bands of interest. Synthetic photometry is important for several reasons. Colors can be computed, as well as absolute magnitudes, which can thus be used to compute bolometric corrections (BC). The variation of the BC with the effective temperature can then be explored. Bolometric corrections are useful to estimate stellar luminosities from photometric surveys.

To compute the absolute magnitudes in each band, we proceeded as follows: each model spectrum of our LMC and SMC grids was first re-scaled from 1 kpc – the CMFGEN output default – to 10 pc. Then, we used each SED as input in the Python package PYPHOT, created by Morgan Fouesneau⁶. The flux points and then magnitudes are computed according to the following formula:

$$M_{\lambda} = -2.5 \times \log \int F_{\lambda} B_{\lambda} d\lambda + \text{const.}$$

where B_{λ} is the filter passband. With the absolute magnitudes, the bolometric corrections follow straightforwardly from:

$$BC_{\lambda} = M_{\odot}^{\text{bol}} - M_{\lambda} - 2.5 \times \log \frac{L}{L_{\odot}}$$

where M_{\odot}^{bol} is the solar bolometric magnitude, equals to 4.75 (IAU 1999), and L/L_{\odot} is the model luminosity in solar units.

We used the Johnson UBV, Cousins RI, and Bessel JHK photometric bands. We also computed magnitudes in some filters from JWST, namely, F070W, F090W, F115W, F150W, and

F200W⁷. This is the first time that JWST absolute magnitudes of models representing OB stars are presented. For the benefit of the Gaia mission we provide G, Gbp, and Grp magnitudes (DR3). Finally, in preparation of the Vera Rubin survey, we calculated magnitudes in the six Legacy Survey of Space and Time (LSST) filters (u, g, r, i, z, and y). Details about all filters used – for example, centers, widths, transmission curves and zero points – can be found at the Spanish Virtual Observatory website (Rodrigo, Solano & Bayo 2012; Rodrigo & Solano 2020)⁸. Figure 5 shows the transmission curves of all filters considered and their relative wavelength position compared to typical SEDs of our grid models. The complete dataset, with all the absolute magnitudes and bolometric corrections in each photometric band, will be available in the VizieR catalog (CDS, Strasbourg).

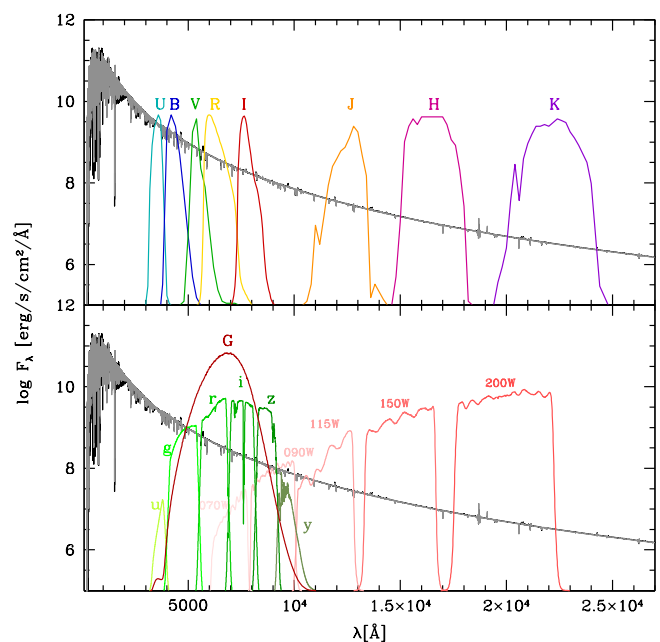


Fig. 5. Illustration of the position of the selected filters for computation of photometry. The top panel shows the Johnson UBV, Cousins RI, and Bessel JHK filters. The bottom panel shows the Gaia G band (dark red), LSST (levels of green) and JWST (levels of pink) filters. GAIA Gbp and Grp filters were omitted, for clarity. Two models at LMC (black) and SMC (grey) metallicity are shown. They both have $T_{\text{eff}} = 37000$ K and $\log g = 3.6$.

Figure 6 shows the distribution of apparent magnitude values (m_{λ} 's) inferred from all synthetic spectra, from both the LMC and SMC grids⁹. A total of 13332 magnitudes are displayed using violin plots. Their shapes illustrate the data density in each band. Medians are indicated by white dots. Thick black bars represent the interquartile ranges, giving an indication of the spread of 50% of the data. Thin lines within each violin represent the range of values.

The classical UBVRIJHK magnitudes are followed by JWST, LSST, and GAIA magnitudes. The apparent magnitudes

⁷ The number is the central wavelength of the filter in $10^{-2}\mu\text{m}$ units and W stands for wide. For more details, see the [JWST User Documentation](http://svo2.cab.inta-csic.es/svo/theory/fps3/).

⁸ <http://svo2.cab.inta-csic.es/svo/theory/fps3/>

⁹ The corresponding plot with absolute magnitudes is obviously similar, the values are merely shifted in the vertical axis by the respective distance moduli.

⁶ <https://mfouesneau.github.io/pyphot/>

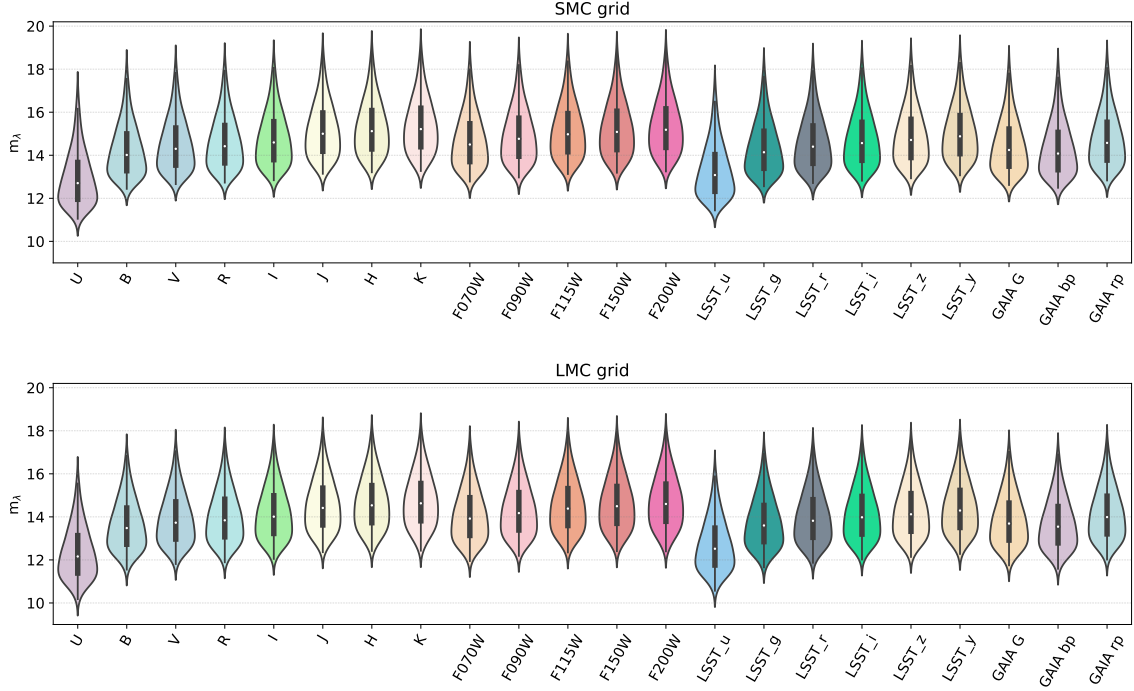


Fig. 6. Synthetic photometry of OB stars in the LMC and SMC, as calculated from our models. We show the distribution of magnitudes in several bands through a violin statistical plot. The adopted distances for the LMC and SMC follow the distance moduli of the LMC and SMC (Pietrzyński et al. 2019; Graczyk et al. 2020; Vink et al. 2023). ISM effects are not taken into account (see text for more details).

Table 2. Fit coefficients for the $BC_{\lambda}-T_{\text{eff}}$ relation at SMC metallicity.

Band	intercept	slope	rms
U	23.32 ± 0.36	-5.53 ± 0.08	0.14
B	25.28 ± 0.28	-6.25 ± 0.06	0.11
V	25.75 ± 0.22	-6.41 ± 0.05	0.08
R	25.87 ± 0.19	-6.46 ± 0.04	0.07
I	26.03 ± 0.17	-6.53 ± 0.04	0.06
J	26.55 ± 0.14	-6.73 ± 0.03	0.05
H	26.62 ± 0.16	-6.77 ± 0.03	0.06
K	26.67 ± 0.18	-6.80 ± 0.04	0.07
F070W	25.92 ± 0.18	-6.49 ± 0.04	0.07
F090W	26.28 ± 0.15	-6.62 ± 0.03	0.06
F115W	26.57 ± 0.14	-6.73 ± 0.03	0.05
F150W	26.58 ± 0.15	-6.73 ± 0.03	0.06
F200W	26.65 ± 0.17	-6.79 ± 0.04	0.07
LSST u	23.79 ± 0.34	-5.72 ± 0.08	0.13
LSST g	25.47 ± 0.26	-6.31 ± 0.06	0.10
LSST r	25.85 ± 0.20	-6.45 ± 0.04	0.07
LSST i	25.98 ± 0.17	-6.51 ± 0.04	0.06
LSST z	26.20 ± 0.15	-6.59 ± 0.03	0.06
LSST y	26.50 ± 0.14	-6.69 ± 0.03	0.05
Gaia G	25.50 ± 0.23	-6.35 ± 0.05	0.09
Gaia Gbp	25.23 ± 0.26	-6.25 ± 0.06	0.10
Gaia Grp	26.01 ± 0.17	-6.52 ± 0.04	0.06

Table 3. Fit coefficients for the $BC_{\lambda}-T_{\text{eff}}$ relation at LMC metallicity.

Band	intercept	slope	rms
U	23.38 ± 0.34	-5.54 ± 0.07	0.12
B	25.22 ± 0.26	-6.23 ± 0.06	0.10
V	25.76 ± 0.21	-6.41 ± 0.05	0.08
R	25.81 ± 0.18	-6.44 ± 0.04	0.07
I	26.01 ± 0.17	-6.52 ± 0.04	0.06
J	26.50 ± 0.15	-6.71 ± 0.03	0.05
H	26.50 ± 0.17	-6.74 ± 0.04	0.06
K	26.41 ± 0.20	-6.74 ± 0.04	0.07
F070W	25.92 ± 0.17	-6.48 ± 0.04	0.06
F090W	26.27 ± 0.15	-6.61 ± 0.03	0.06
F115W	26.49 ± 0.14	-6.71 ± 0.03	0.05
F150W	26.50 ± 0.16	-6.73 ± 0.03	0.06
F200W	26.41 ± 0.20	-6.73 ± 0.04	0.07
LSST u	23.83 ± 0.32	-5.72 ± 0.07	0.12
LSST g	25.43 ± 0.24	-6.30 ± 0.05	0.09
LSST r	25.81 ± 0.19	-6.44 ± 0.04	0.07
LSST i	25.96 ± 0.17	-6.50 ± 0.04	0.06
LSST z	26.18 ± 0.16	-6.58 ± 0.03	0.06
LSST y	26.45 ± 0.14	-6.68 ± 0.03	0.05
Gaia G	25.48 ± 0.22	-6.33 ± 0.05	0.08
Gaia Gbp	25.18 ± 0.24	-6.24 ± 0.05	0.09
Gaia Grp	26.02 ± 0.16	-6.52 ± 0.04	0.06

were computed from the equation $m_{\lambda} = M_{\lambda} - 5 + 5 \times \log d$, using the distances of the LMC and SMC. ISM effects are not taken into account.

Overall, the distributions increase in magnitude from blue to redder filters, as expected. Moreover, they possess similar

shapes, without anomalies (e.g., skewness, multiple peaks), indicating that the models and flux calculations were carried out properly. Fig. 6 also provides a graphical visualization of apparent magnitudes that massive OB stars in the Magellanic Clouds may have in each band, in case of minimal or no extinction line

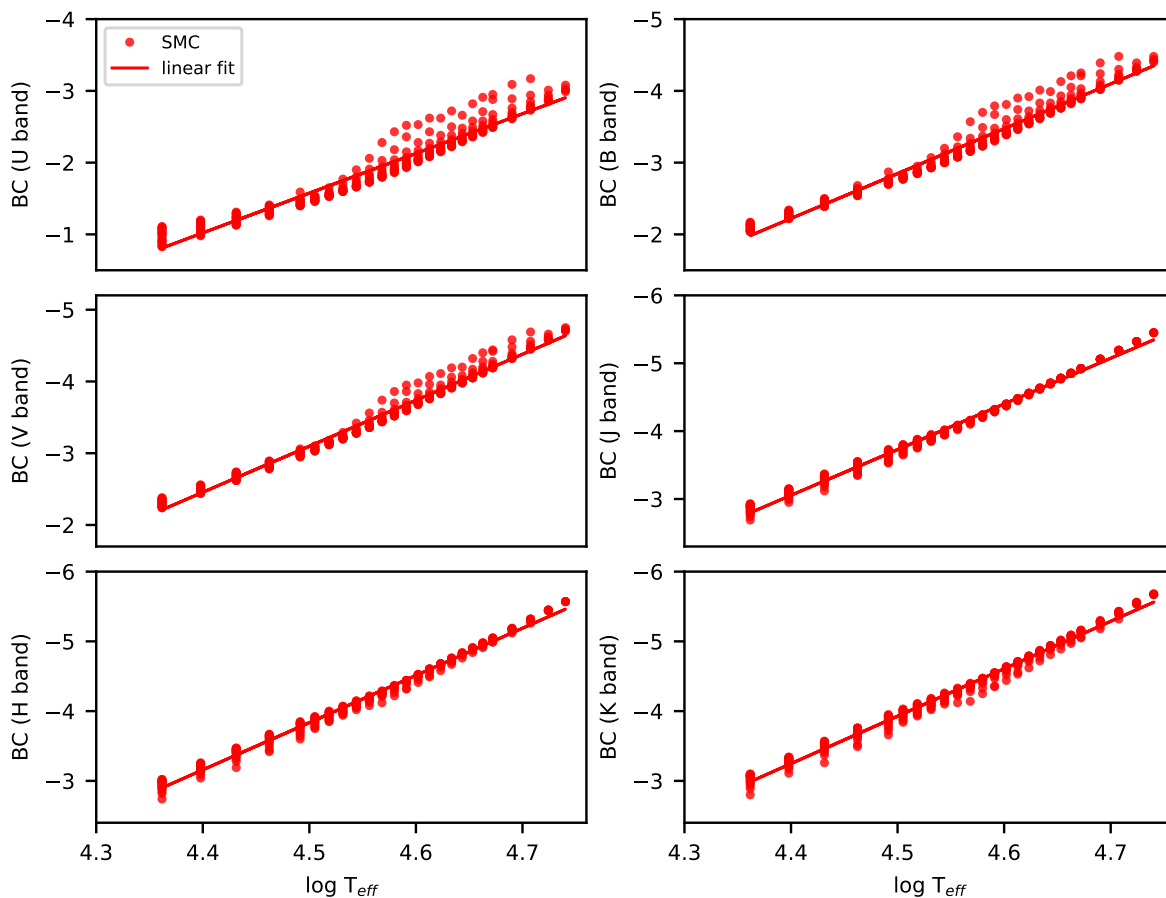


Fig. 7. Bolometric corrections versus the effective temperature in selected photometric bands (see text for details). Our SMC data is indicated by solid circles and the corresponding linear fit by a solid line.

of sights. However, the distributions shown serve as indicators rather than definitive representations. For real objects, the distributions are expected to be shifted differentially and upwards (by $m_{\lambda} + A_{\lambda}$). The position of the medians could also be affected, since some spectral types are more abundant than others (e.g., through the IMF and observational biases).

Figure 7 shows the bolometric corrections in the most used, classical UBVIJK bands, as a function of the effective temperature. Only the SMC points are displayed. Nevertheless, we provide in Tables 2 and 3 the coefficients of the linear relations for all bands, for the SMC and LMC, respectively.

The absolute values of the bolometric corrections increase with temperature, as expected. Indeed, using the Wien maximum as a first approximation, the peak of the spectral energy distribution occurs at shorter wavelengths for higher effective temperatures. For instance, at approximately 1159\AA for $\log T_{\text{eff}} \sim 4.4$ ($\sim 25000\text{K}$) and at $\sim 580\text{\AA}$, for $\log T_{\text{eff}} \sim 4.7$ ($\sim 50000\text{K}$). Therefore, this peak shifts away from the wavelength centers of the different filters we consider as we go towards high effective temperatures, meaning higher bolometric corrections.

The effective temperature is not the only parameter that influences the bolometric corrections. For the U, B and V bands at $\log T_{\text{eff}} \sim 4.6$, for example, there is a spread of BC values. This is a natural consequence of the way our grids were constructed.

For a specific temperature, we explored different values of surface gravities and luminosities and thus mass-loss rates, affecting the photometry (see Sect. 2).

Martins & Plez (2006) provide a calibration of bolometric correction versus T_{eff} for Galactic stars. It is tempting to compare directly the present results to this calibration to investigate metallicity effects. However this task is rather complex for the following reasons. First, Martins & Plez (2006) used generic Johnson filters as we do in this work for UBVI bands, but the exact shape of the transmission curve and the associated zero points are not strictly the same. This leads to systematic variations in photometry. Second, the present models are more complete than those of Martins & Plez (2006). In particular, we include more elements, levels, and lines. The resulting line-blanking effects that affect the shape of the SED are thus not of the same order in the two studies. This introduces another source of potential difference in synthetic photometry. Third, we assume that the relations between bolometric corrections and $\log(T_{\text{eff}})$ are linear. Inspection of Figs. 7 reveals that this is a very good assumption for some temperature ranges, but only approximate for the full interval. Depending on the range of T_{eff} considered, the coefficients of the linear regressions vary. As an example, restricting the T_{eff} range to $30000\text{--}45000\text{ K}$ leads to $BC(V) = 28.86 - 7.07 \times \log(T_{\text{eff}})$. This is significantly steeper than the relation reported in Table 3.

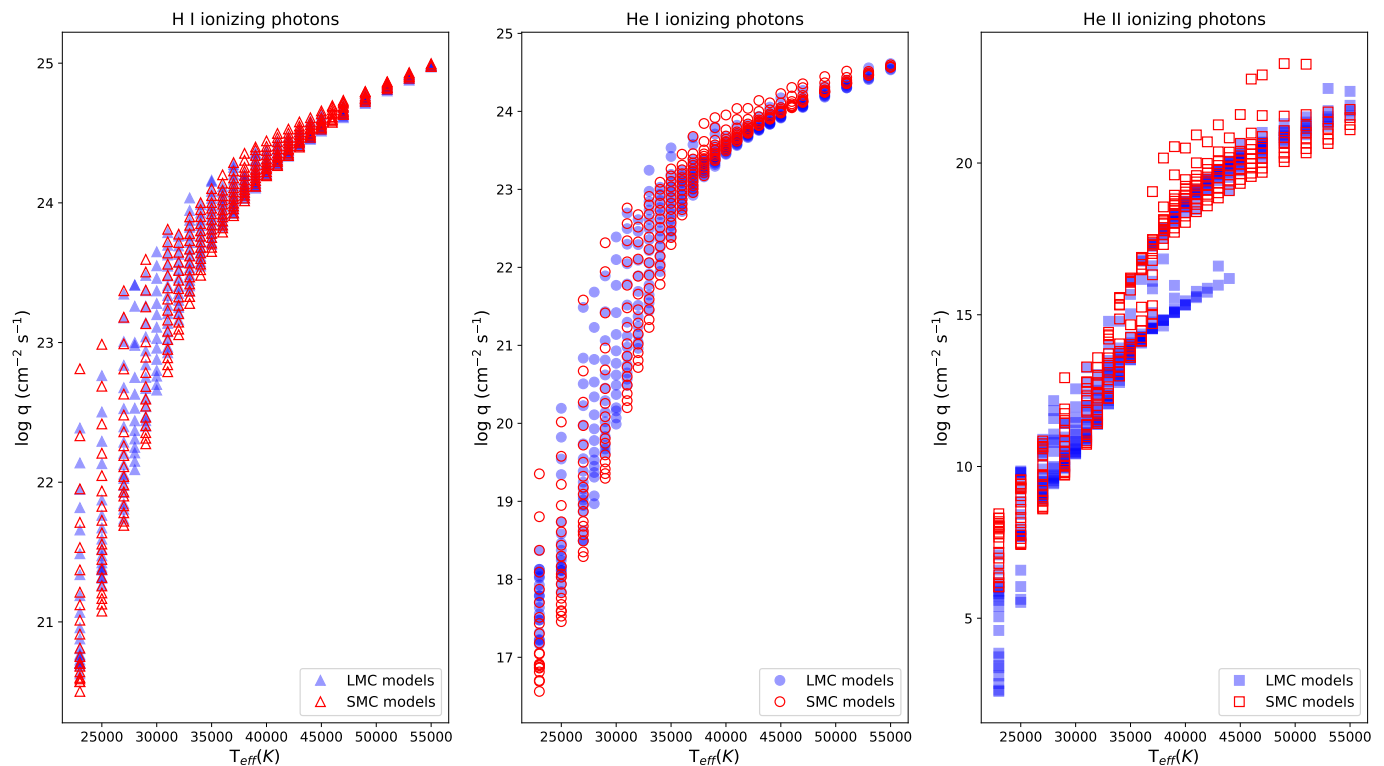


Fig. 8. Logarithm of the number of ionizing photons per unit surface area ($\log q$) as a function of the effective temperature from our grid models. From left to right we show $\log q$ above the ionization threshold for H I, He I, and He II. Red (blue) points represent the SMC (LMC) grid.

Since the relations of [Martins & Plez \(2006\)](#) are based on models that cover a narrower range of T_{eff} than the present study, a direct comparison between their and our relations cannot provide any insight into the metallicity dependence of bolometric corrections.

However, what is feasible is a comparison between the SMC and LMC relations of the present study, since they rely on the same photometric set-up and on grids that cover the same parameter space. Tables 2 and 3 show that for a given T_{eff} bolometric corrections are very similar, hinting at the absence of metallicity effect between the SMC and the LMC. In fact, the slopes and intercepts in each band are compatible between the LMC and SMC cases within the uncertainties.

We would like to remind readers that line-blanketing and thus back-warming, as well as flux redistribution, change the SED of models with different metallicities. However, our results indicate that to possibly observe significant differences in the BCs and thus in the calibrations, one has to consider a larger Z span (e.g., MW versus SMC or even lower Z).

3.3. Ionizing fluxes

The ionizing radiation from massive stars has a tremendous impact on their surroundings. As such, it is a key concept that connects stellar and extragalactic astrophysics subjects. A proper interpretation of stellar populations in local and distant starburst galaxies, for example, relies heavily on their massive star content, evolution, and corresponding ionizing photons output. In a cosmological context, the reionization of the Universe ($z \sim 10 - 12$) is also linked to the amount of ionizing photons produced by the first hot massive stars, a fraction of which was able to escape their host galaxies (see the review by [Eldridge & Stanway 2022](#)).

Robust predictions require computationally expensive, heavily blanketed NLTE expanding atmosphere models. Both the amount of metals and wind presence affect the shape of the spectral energy distribution, changing the number of ionizing photons. Our LMC and SMC grid models were tailored with these considerations.

We have computed the number of ionizing photons Q for the ionization thresholds of H I, He I, and He II, for all models. Q is defined as follows:

$$Q = \int_{\nu_0}^{+\infty} \frac{L_\nu}{h\nu} d\nu,$$

where ν_0 is the frequency threshold for ionization (e.g., of H I), L_ν is the stellar luminosity at frequency ν , and h the Planck constant.

In Fig. 8, we present $\log q$ ($= \log Q/4\pi R^2$) against the effective temperature, which is the main parameter dictating the peak of the flux distribution (see Fig. 2). We chose to present q 's (per unit surface area) instead of Q 's to ensure a meaningful comparison between models. Note that for a few temperatures we have just LMC or SMC models (e.g., at 28000 K).

The number of ionizing photons naturally increases with temperature, as expected. The behavior of ionizing fluxes as a function of metallicity have been discussed by [Martins & Palacios \(2021\)](#) and we refer the reader to their Section 4.1 for details. Briefly we see that $q(\text{H I})$ does not change with metallicity, while $q(\text{He I})$ reaches slightly larger values at lower Z .

The behavior of $q(\text{He II})$ is more complex. [Schmutz & Hamann \(1986\)](#), [Hillier \(1987\)](#), [Gabler et al. \(1989\)](#) and [Schaerer & de Koter \(1997\)](#) provide an explanation for the sensitivity of He II ionizing fluxes to stellar parameters. He II opacity depends on the ground state population that is controlled by temperature

and wind density. For high temperatures and low wind density, He II is fully ionized and the ground state population is low: there is little absorption and the He II flux is high. If wind density increases, the line formation depth is pushed outward in regions where the velocity field is non-negligible. The He II resonance line is shifted so it can absorb more photons, depopulating even more the ground level: the He II flux increases accordingly. When the wind becomes strong enough, recombinations dominate over the latter effect and the ground state becomes over-populated: the He II flux is severely reduced. This general effect has been described by Schaerer & de Koter (1997) and is illustrated in Fig. 13 of Martins & Palacios (2021). It explains the bimodal distribution of $q(\text{He II})$ at LMC metallicity: depending on the mass-loss rate, the He II ionizing flux is either high or low. This can be seen in Fig. 8, at $T_{\text{eff}} \sim 40\text{kK}$, for the LMC points (rightmost panel). At SMC metallicity, winds remain weak enough in our grid so that the bimodal distribution is barely seen. Obviously, at lower T_{eff} ionization is not high enough and the He II opacity is always large. Given this behavior, we stress that the predicted He II depend on the assumptions regarding mass loss and clumping. The presence of X-ray emission caused by shocks in the winds may also affect the He II ionizing fluxes. Hence the absolute values of $q(\text{He II})$ we provide should be regarded as only indicative.

4. Summary and conclusions

We have presented two grids of synthetic spectra computed with the NLTE atmosphere code CMFGEN. These grids cover the Main Sequence (and slightly beyond) of massive stars at metallicities of $1/2 Z_{\odot}$ (LMC) and $1/5 Z_{\odot}$ (SMC). They serve as an alternative to existing ones in the literature, built with different codes (e.g., Lanz & Hubeny 2003, 2007; Todt et al. 2015; Eldridge et al. 2017).

The models are comprehensive in terms of atomic data, with an appropriate amount of metal line blanketing for the analysis of OB stars (see Sect. 2.3). A total of 606 spectra were calculated, from 30 \AA to $3 \mu\text{m}$. We provide flux-calibrated as well as normalized spectra in the UV, optical, and infrared ranges. They are publicly available at the POLLUX database.

In addition to spectroscopic data, we have computed photometry in various filters, including Johnson UB_V, Cousins RI, Bessel JHK, JWST wide, Gaia, and LSST ugrizy filters. We provide bolometric corrections for all bands and their calibration as a function of effective temperature. Finally, we computed H I, He I, and He II ionizing fluxes for all models.

The results and data described here are relevant for the quantitative analysis of the UV and optical spectra provided by the ULLYSES and XSHOOTER observational programs and other future initiatives (e.g., infrared). They can also be used in population synthesis models, to study the nebular properties of H II regions, to characterize new populations of massive OB stars uncovered by photometric surveys, and on hydrodynamic calculations. Our work also serves as a starting point for developing CMFGEN-based grids at even lower metallicities.

Acknowledgements. This research has made use of the Spanish Virtual Observatory (<https://svo.cab.inta-csic.es>) project funded by MCIN/AEI/10.13039/501100011033/ through grant PID2020-112949GB-I00.

References

Aadland, E., Massey, P., Hillier, D. J., et al. 2022, *ApJ*, 931, 157
 Asplund, M., Grevesse, N., Sauval, A. J., & Scott, P. 2009, *ARA&A*, 47, 481

Bernini-Peron, M., Marcolino, W. L. F., Sander, A. A. C., et al. 2023, *A&A*, 677, A50
 Björklund, R., Sundqvist, J. O., Puls, J., & Najarro, F. 2021, *A&A*, 648, 36
 Blondin, S., Dessart, L., & Hillier, D. J. 2015, *MNRAS*, 448, 2766
 Bouret, J.-C., Hillier, D. J., Lanz, T., & Fullerton, A. W. 2012, *A&A*, 544, A67
 Bouret, J.-C., Lanz, T., & Hillier, D. J. 2005, *A&A*, 438, 301
 Bouret, J.-C., Lanz, T., Hillier, D. J., et al. 2003, *ApJ*, 595, 1182
 Bouret, J.-C., Lanz, T., Martins, F., et al. 2013, *A&A*, 555, A1
 Bouret, J. C., Martins, F., Hillier, D. J., et al. 2021, *A&A*, 647, A134
 Castor, J. I., Abbott, D. C., & Klein, R. I. 1975, *ApJ*, 195, 157
 Cioni, M., R. L., Storm, J., Bell, C. P. M., et al. 2019, *The Messenger*, 175, 54
 Crowther, P. A., Lennon, D. J., & Walborn, N. R. 2006, *A&A*, 446, 279
 de Almeida, E. S. G., Marcolino, W. L. F., Bouret, J. C., & Pereira, C. B. 2019, *A&A*, 628, A36
 de Burgos, A., Simón-Díaz, S., Urbaneja, M. A., & Negueruela, I. 2023, *A&A*, 674, A212
 Dessart, L. & Hillier, D. J. 2005, *A&A*, 437, 667
 Dessart, L. & Hillier, D. J. 2015, *MNRAS*, 447, 1370
 Dessart, L., Hillier, D. J., Woosley, S. E., & Kuncarayakti, H. 2023, *A&A*, 677, A7
 Eggenberger, P., Ekström, S., Georgy, C., et al. 2021, *A&A*, 652, A137
 Eldridge, J. J. & Stanway, E. R. 2022, *ARA&A*, 60, 455
 Eldridge, J. J., Stanway, E. R., Xiao, L., et al. 2017, *PASA*, 34, e058
 Flores, B. L. & Hillier, D. J. 2021, *MNRAS*, 504, 311
 Flores, B. L., Hillier, D. J., & Dessart, L. 2023, *MNRAS*, 518, 5001
 Gabler, R., Gabler, A., Kudritzki, R. P., Puls, J., & Pauldrach, A. 1989, *A&A*, 226, 162
 Georgy, C., Ekström, S., Eggenberger, P., et al. 2013, *A&A*, 558, A103
 Graczyk, D., Pietrzyński, G., Thompson, I. B., et al. 2020, *ApJ*, 904, 13
 Gräfener, G., Koesterke, L., & Hamann, W. R. 2002, *A&A*, 387, 244
 Groh, J. H., Hillier, D. J., & Damineli, A. 2011, *ApJ*, 736, 46
 Groh, J. H., Hillier, D. J., Damineli, A., et al. 2009, *ApJ*, 698, 1698
 Hainich, R., Ramachandran, V., Shenar, T., et al. 2019, *A&A*, 621, A85
 Hawcroft, C., Sana, H., Mahy, L., et al. 2024, *A&A*, 688, 105
 Heap, S. R., Lanz, T., & Hubeny, I. 2006, *ApJ*, 638, 409
 Hillier, D. J. 1987, *ApJS*, 63, 947
 Hillier, D. J. 2012, in *From Interacting Binaries to Exoplanets: Essential Modeling Tools*, ed. M. T. Richards & I. Hubeny, Vol. 282, 229–234
 Hillier, D. J. 2020, *Galaxies*, 8, 60
 Hillier, D. J., Lanz, T., Heap, S. R., et al. 2003, *ApJ*, 588, 1039
 Hillier, D. J. & Miller, D. L. 1998, *ApJ*, 496, 407
 Hillier, D. J. & Miller, D. L. 1999, *ApJ*, 519, 354
 Holgado, G., Simón-Díaz, S., Barbá, R. H., et al. 2018, *A&A*, 613, A65
 Hubeny, I. & Lanz, T. 1995, *ApJ*, 439, 875
 Hunter, I., Brott, I., Lennon, D. J., et al. 2008, *ApJ*, 676, L29
 Hutchings, J. B. 1976, *ApJ*, 204, L99
 Hutchings, J. B. & von Rudloff, I. R. 1980, *ApJ*, 238, 909
 Krtićka, J., Kubát, J., & Krtićková, I. 2024, *A&A*, 681, 29
 Kudritzki, R. P., Pauldrach, A., Puls, J., & Abbott, D. C. 1989, *A&A*, 219, 205
 Lanz, T. & Hubeny, I. 2003, *ApJS*, 146, 417
 Lanz, T. & Hubeny, I. 2007, *ApJS*, 169, 83
 Leitherer, C., Robert, C., & Drissen, L. 1992, *ApJ*, 401, 596
 Lucy, L. B. & Solomon, P. M. 1970, *ApJ*, 159, 879
 Mahy, L., Sana, H., Abdul-Masih, M., et al. 2020, *A&A*, 634, A118
 Marcolino, W. L. F., Bouret, J. C., Lanz, T., Maia, D. S., & Audard, M. 2017, *MNRAS*, 470, 2710
 Marcolino, W. L. F., Bouret, J.-C., Martins, F., et al. 2009, *A&A*, 498, 837
 Marcolino, W. L. F., Bouret, J. C., Rocha-Pinto, H. J., Bernini-Peron, M., & Vink, J. S. 2022, *MNRAS*, 511, 5104
 Marcolino, W. L. F., de Araújo, F. X., Junior, H. B. M., & Duarte, E. S. 2007a, *AJ*, 134, 1380
 Marcolino, W. L. F., Hillier, D. J., de Araujo, F. X., & Pereira, C. B. 2007b, *ApJ*, 654, 1068
 Markova, N., Puls, J., & Langer, N. 2018, *A&A*, 613, A12
 Markova, N., Puls, J., Simón-Díaz, S., et al. 2014, *A&A*, 562, A37
 Martins, F., Bouret, J. C., Hillier, D. J., et al. 2024, *A&A*, in press
 Martins, F., Hervé, A., Bouret, J.-C., et al. 2015, *A&A*, 575, A34
 Martins, F. & Palacios, A. 2017, *A&A*, 598, A56
 Martins, F. & Palacios, A. 2021, *A&A*, 645, A67
 Martins, F. & Palacios, A. 2022, *A&A*, 659, A163
 Martins, F. & Plez, B. 2006, *A&A*, 457, 637
 Martins, F., Schaerer, D., & Hillier, D. J. 2002, *A&A*, 382, 999
 Martins, F., Schaerer, D., & Hillier, D. J. 2005, *A&A*, 436, 1049
 Martins, F., Schaerer, D., Hillier, D. J., & Heydari-Malayeri, M. 2004, *A&A*, 420, 1087
 Martins, F., Schaerer, D., Marques-Chaves, R., & Upadhyaya, A. 2023, *A&A*, 678, A159
 Mokiem, M. R., de Koter, A., Evans, C. J., et al. 2006, *A&A*, 456, 1131
 Mokiem, M. R., de Koter, A., Vink, J. S., et al. 2007, *A&A*, 473, 603
 Morris, P. W., Gull, T. R., Hillier, D. J., et al. 2017, *ApJ*, 842, 79

- Morton, D. C. 1967, *ApJ*, 147, 1017
- Neugent, K. F., Massey, P., Hillier, D. J., & Morrell, N. 2017, *ApJ*, 841, 20
- Palacios, A., Gebran, M., Josselin, E., et al. 2010, *A&A*, 516, A13
- Pauldrach, A. W. A., Feldmeier, A., Puls, J., & Kudritzki, R. P. 1993, *Space Sci. Rev.*, 66, 105
- Pauldrach, A. W. A., Hoffmann, T. L., & Lennon, M. 2001, *A&A*, 375, 161
- Pietrzyński, G., Graczyk, D., Gallenne, A., et al. 2019, *Nature*, 567, 200
- Puls, J., Springmann, U., & Lennon, M. 2000, *A&AS*, 141, 23
- Ramírez-Agudelo, O. H., Simón-Díaz, S., Sana, H., et al. 2013, *A&A*, 560, A29
- Repolust, T., Puls, J., & Herrero, A. 2004, *A&A*, 415, 349
- Sander, A., Hamann, W. R., & Todt, H. 2012, *A&A*, 540, A144
- Sander, A., Shenar, T., Hainich, R., et al. 2015, *A&A*, 577, A13
- Schaerer, D. & de Koter, A. 1997, *A&A*, 322, 598
- Schmutz, W. & Hamann, W. R. 1986, *A&A*, 166, L11
- Searle, S. C., Prinja, R. K., Massa, D., & Ryans, R. 2008, *A&A*, 481, 777
- Shenar, T., Bodensteiner, J., Sana, H., et al. 2024, *A&A*, submitted
- Snow, T. P., J. & Morton, D. C. 1976, *ApJS*, 32, 429
- Teodoro, M., Gull, T. R., Bautista, M. A., et al. 2020, *MNRAS*, 495, 2754
- Todt, H., Sander, A., Hainich, R., et al. 2015, *A&A*, 579, A75
- Vink, J. S., de Koter, A., & Lamers, H. J. G. L. M. 2001, *A&A*, 369, 574
- Vink, J. S., Mehner, A., Crowther, P. A., et al. 2023, *A&A*, 675, A154
- Zsargó, J., Fierro-Santillán, C. R., Klapp, J., et al. 2020, *A&A*, 643, A88

Appendix A: Appendix

Appendix A.1: UV spectra

Figure A.1 displays examples of spectra in the UV/EUV range, to highlight the role and the richness of the iron forest, and the effects of differing metallicities.

For each metallicity, we selected two effective temperatures, namely $T_{\text{eff}} = 35000$ K and $T_{\text{eff}} = 51000$ K. For visualization purposes, the spectra were normalized and convolved with an arbitrary rotational velocity of 30 km s^{-1} . The wavelength interval is $500 - 2000 \text{ \AA}$. Besides the full spectra at the bottom of the two panels, we provide the spectra of individual iron ions, revealing their respective contributions.

At $T_{\text{eff}} = 35000$ K, Fe IV-V dominate. At $T_{\text{eff}} = 51000$ K, the wind ionization is higher and Fe V-VI dominate. Figure A.1 clearly shows the significant reduction in absorption strengths of iron lines at lower metallicity (SMC). These plots suggest that a careful analysis of the variation of Fe ions and lines with temperature might provide a useful tool to constrain T_{eff} (see Heap et al. 2006, for a first attempt), i.e., independently from the usual helium and/or silicon optical lines in OB stars (see e.g., de Almeida et al. 2019; Bernini-Peron et al. 2023; Crowther et al. 2006).

The P-Cygni profiles of CNO lines are obviously affected by the global model metallicity (the metal abundances are scaled-solar). They present important variations (see for instance, C IV $\lambda 1549$ at $T_{\text{eff}} = 51$ kK). However, we recall that the models have been calculated with wind parameters obtained using the Vink formula (Vink et al. 2001), which implicitly scales M and v_{∞} to the adopted metallicity. On the other hand, the Ly α wind line remains unchanged, being from hydrogen and saturated (bottom panel).

Appendix A.2: Optical spectra

The optical spectra of our grids can be used to infer the surface gravity and effective temperature of an observed star. We present in Fig. A.2 examples of models with a fixed surface gravity and various T_{eff} values and vice-versa. The spectra were convolved with a resolving power $R = 5000$. We selected the lines H γ , He I $\lambda 4471$, and He II $\lambda 4542$. They have been canonically used for years as diagnostic lines in O stars¹⁰. However, ideally, various helium and hydrogen lines should be utilized simultaneously.

The leftmost panels illustrates the changes on the wings of H γ when the surface gravity is varied. The effective temperature is fixed at 40 kK. The $\log g$ goes from 3.5 to 4.1 in steps of 0.2 dex. When compared with a high signal-to-noise observed spectrum, the changes observed are usually enough for the choice of a best model. An accuracy of 0.1-0.2 dex is commonly obtained in the modeling of high-resolution spectra (see e.g., Bouret et al. 2012, 2013).

The middle and rightmost panels show the effect of varying the effective temperature. The surface gravity is fixed at $\log g = 3.8$. The He I line changes drastically, while the He II changes are more modest. In practice, T_{eff} can be inferred with 1-2 kK accuracy (see e.g., Bouret et al. 2012, 2013).

Appendix A.3: Infrared spectra

We present selected infrared spectra in Fig. A.3. Here, we chose only LMC models. The wavelength interval is $0.85 - 2.25 \text{ \mu m}$. We convolved all spectra with $R=2700$, for visualization purposes. This resolving power is, for instance, compatible with the JWST NIRSpec instrument in this spectral range (disperser-filter G140H/F100LP and G235H/F170LP). Two effective temperatures are shown, namely, 35kK and 55kK. The surface gravity is $\log g = 4.0$. Individual contributions from hydrogen and helium are displayed above the full spectrum in each panel. Most hydrogen lines correspond to the Paschen ($j \rightarrow 3$) and Brackett ($j \rightarrow 4$) series. Note the shift in the He I/He II ratio in the two temperatures. High temperature models do not possess He I transitions in the wavelength interval shown.

¹⁰ For B stars, Si II-IV, He I, and Mg II lines can be used to infer the effective temperature, while Balmer line wings allows the determination of $\log g$ (see e.g., Crowther et al. 2006; Searle et al. 2008; Bernini-Peron et al. 2023)

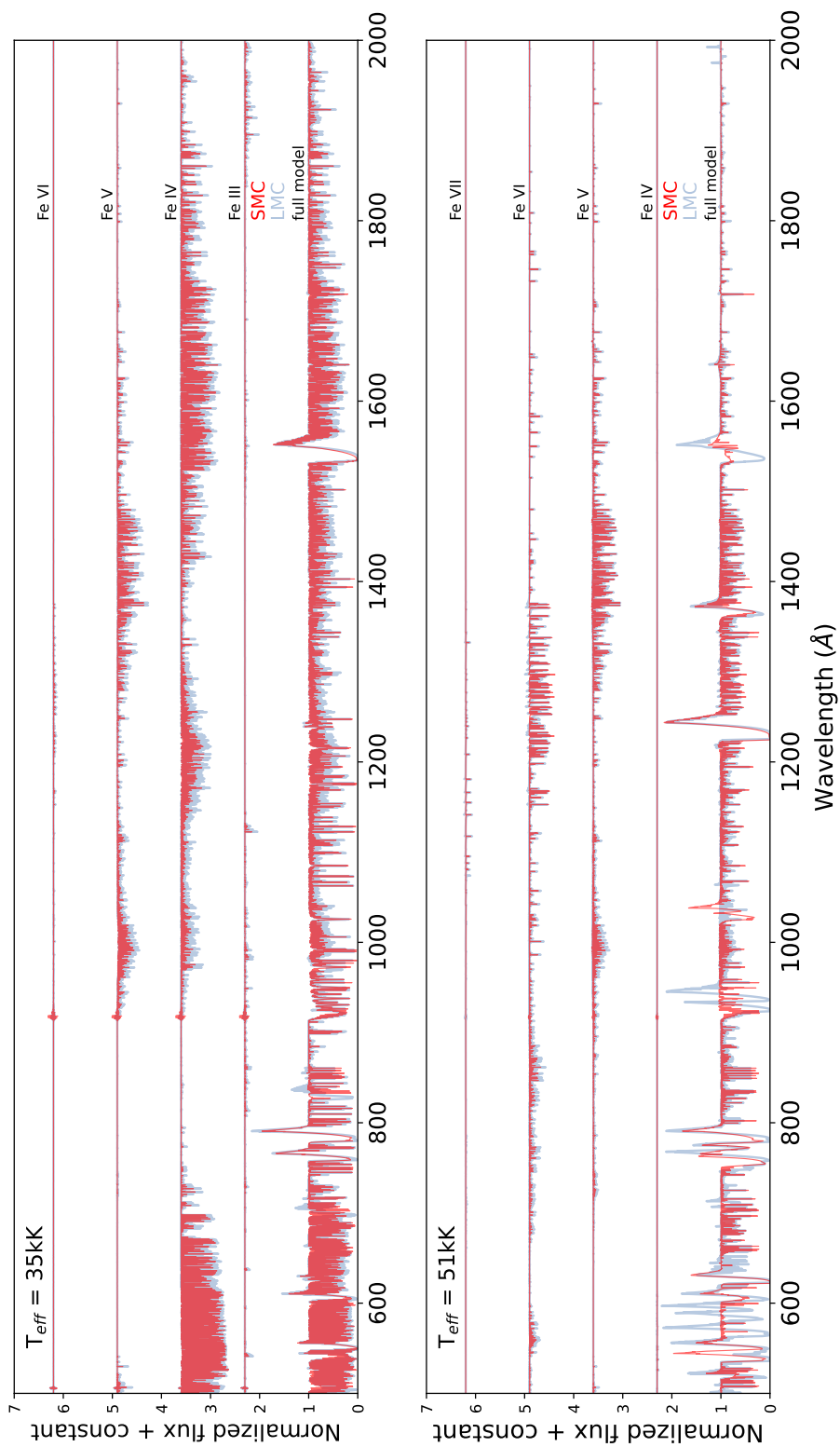


Fig. A.1. Ultraviolet spectra: iron forest and metallicity effect. Two models for each temperature are presented: one with $0.5 Z_{\odot}$ (LMC; gray) and the other with $0.2 Z_{\odot}$ (SMC; red). The surface gravity is $\log g = 4.0$ and the luminosity is $\log L/L_{\odot} = 4.8$ for the $T_{\text{eff}} = 35$ kK models. The surface gravity is $\log g = 5.9$ (SMC) and $\log L/L_{\odot} = 6.1$ (LMC) for the $T_{\text{eff}} = 51$ kK models. Wind parameters are adopted using the Vink formula (Vink et al. 2001). The full spectra are displayed at the bottom of each panel, while individual contributions of iron ions are shown above. Note the variations in the prevalence of iron ions and the significant reduction in absorption between the SMC and LMC models.

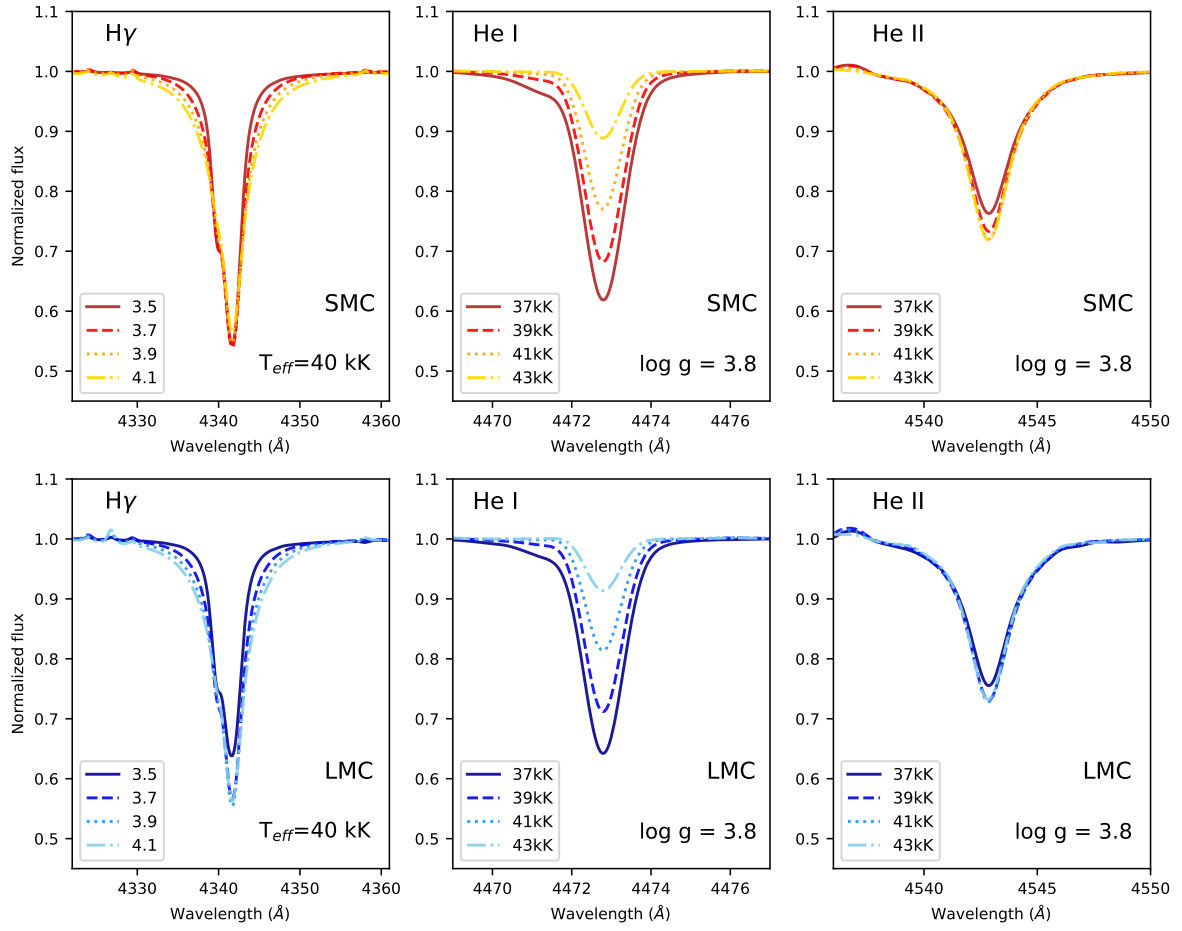


Fig. A.2. Classical effects arising from variations in $\log g$ and T_{eff} on optical spectra, as depicted by our grid models. Top panel: SMC models. Lower panel: LMC models. The chosen helium lines are: He I $\lambda 4471$ and He II $\lambda 4542$. They are often used with other He I-II lines to infer T_{eff} in O stars, usually with a 1-2 kK uncertainty. The surface gravity determination from H γ (and other Balmer lines) has a typical uncertainty of 0.1-0.2 dex. The effective temperature is fixed in the leftmost panels and the $\log g$ is varied (see caption). The other panels have $\log g$ fixed and the effective temperature is varied (see caption).

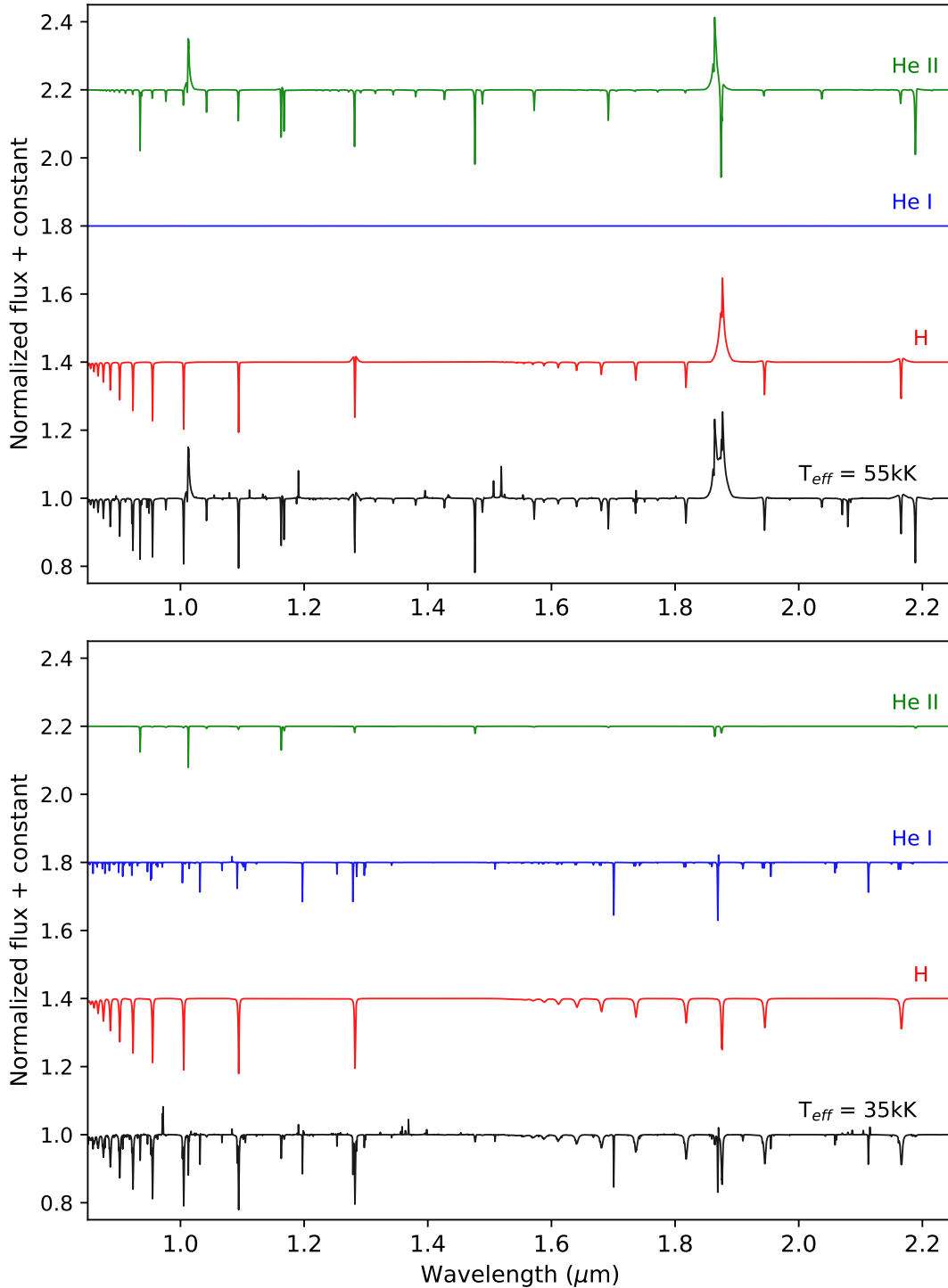


Fig. A.3. Examples of infrared spectra at 0.85–2.25 μm (LMC metallicity). Top panel: model with $T_{\text{eff}} = 55\text{ kK}$ and $\log g = 4.0$. Bottom panel: model with $T_{\text{eff}} = 35\text{ kK}$ and $\log g = 4.0$. The spectra were convolved with $R = 2700$, appropriate, for example, for JWST NIRSpec data. In each panel, the full spectrum is shown at the bottom (black) and individual H I, He I, and He II contributions are denoted above.